

SYNTHETIC SPECTRA OF RADIO, MILLIMETER, SUB-MILLIMETER, AND INFRARED REGIMES WITH NON-LOCAL THERMODYNAMIC EQUILIBRIUM APPROXIMATION

VICTOR DE LA LUZ^{1,2}, ALEJANDRO LARA¹, AND JEAN-PIERRE RAULIN³

¹ Instituto de Geofísica, Universidad Nacional Autónoma de México 04510, Mexico

² Instituto Nacional de Astrofísica, Óptica y Electrónica, Tonantzintla, Puebla, Apdo. Postal 51 y 216, 72000, Mexico

³ CRAAM, Universidade Presbiteriana Mackenzie, São Paulo, SP, 01302-907, Brazil

Received 2011 March 29; accepted 2011 May 12; published 2011 July 19

ABSTRACT

We use a numerical code called PAKALMPI to compute synthetic spectra of the solar emission in quiet conditions at millimeter, sub-millimeter, and infrared wavelengths. PAKALMPI solves the radiative transfer equation, with non-local thermodynamic equilibrium (NLTE), in a three-dimensional geometry using a multiprocessor environment. The code is able to use three opacity functions: classical bremsstrahlung, H^- , and inverse bremsstrahlung. In this work, we have computed and compared two synthetic spectra, one in the common way: using bremsstrahlung opacity function and considering a fully ionized atmosphere; and a new one considering bremsstrahlung, inverse bremsstrahlung, and H^- opacity functions in NLTE. We analyzed in detail the local behavior of the low atmospheric emission at 17, 212, and 405 GHz (frequencies used by the Nobeyama Radio Heliograph and the Solar Submillimeter Telescope). We found that the H^- is the major emission mechanism at low altitudes (below 500 km) and that at higher altitudes the classical bremsstrahlung becomes the major mechanism of emission. However, the brightness temperature remains unalterable. Finally, we found that the inverse bremsstrahlung process is not important for radio emission at these heights.

Key words: methods: numerical – radiation mechanisms: thermal – radiative transfer – Sun: atmosphere – Sun: chromosphere – Sun: radio radiation

Online-only material: color figures

1. INTRODUCTION

The radio emission from astronomical sources may be a powerful tool to study the physical conditions of the source and the medium between it and the observer. In particular at centimetric, millimetric, and sub-millimetric wavelengths, the radio emission from the solar atmosphere carries out valuable information from the physical conditions of the chromosphere and the transition region.

The solar emission at high radio frequencies can be explained by two major solar regimes: the flaring case, where non-thermal emission from accelerated electrons and thermal emission from hot and cold plasmas are the main processes; and the quiet-Sun regime, where the emission is attributed to thermal bremsstrahlung (Kundu 1970), for which the magnetic field is not directly important. Note that the magnetic field structures matter in the solar atmosphere, therefore it will influence the plasma density structure, for instance, in the case of chromospheric spicules.

In the early 1930s, the first attempts were made to explain the solar chromosphere (Cillié & Menzel 1935). But it was only after the eclipse observations of 1952 that the existence of a two-component model in temperature was established (hot and cold model suggested by Giovanelli 1949).

The classical treatment of the solar chromosphere in the quiet regime is based on the assumption that the atmosphere is static and in hydrostatic equilibrium (Vernazza et al. 1973). Also, the radio and UV spectra must be in agreement, therefore in several works the relationship between the UV line emission and the continuum at millimeter and sub-millimeter wavelengths have been studied (Kuznetsova 1978; Ahmad & Kundu 1981; Chiuderi Drago et al. 1983; Landi & Chiuderi Drago 2003;

Loukitcheva et al. 2004; Chiuderi & Chiuderi Drago 2004; de La Luz et al. 2008).

By assuming an emission mechanism, the observed radio spectrum can be correlated with the atmospheric height of the source (Vernazza et al. 1976; Ayres 1989; Avrett & Loeser 2008; De la Luz et al. 2010). Generally, the height associated with a specific emitting frequency is the height of the layer where the atmosphere becomes optically thick. However, the transition between optically thin ($\tau_\nu \ll 1$) and optically thick regimes ($\tau_\nu \gg 1$) is quite ambiguous.

Theoretically, the solar emission can be modeled by solving the radiative transfer equation taking into account the temperature and density of the solar atmosphere, and using the required opacity functions in accordance with the relevant photon–particle interactions. In particular, from millimeter to infrared wavelengths range, the free–free interaction (bremsstrahlung) is the main mechanism used to reproduce solar spectra (Dulk 1985; Raulin & Pacini 2005), and, also, a fully ionized atmosphere is commonly assumed. With these assumptions both the time and the complexity of the computations are greatly reduced, specially for the quiet-Sun emission case.

It is clear that more photon–particle interactions take place in the solar atmosphere; in particular, the H^- continuum provides the dominant radiation at photospheric level (Athay & Thomas 1961) and therefore H^- must be considered as an important source of sub-millimeter and infrared emission at low chromospheric level. We expect that the interactions between H^- and free electrons (inverse bremsstrahlung; Golovinskii & Zon 1980) are important at this wavelength range also.

Therefore, in order to reproduce a more realistic solar spectra, it is necessary to compute explicitly the density of the different ion species and feed with this information the

relevant opacity functions, using non-local thermodynamical equilibrium (NLTE). In this way, we have constructed a synthetic spectrum of the solar quiescent radio emission at short wavelengths.

As a first step, we compute the ion and electron density at any layer of the atmosphere using as inputs atomic models and pre-calculated density and temperature atmospheric profiles for the quiet-Sun regime. Then, we solve the radiative transfer equation for the required ray paths. We use PAKALMPI, an updated version of the PAKAL code (De la Luz et al. 2010) to compute a synthetic spectrum of the solar emission from millimeter to infrared wavelengths. PAKALMPI solves the radiative transfer equation, in NLTE conditions, in a three-dimensional geometry using a multiprocessor environment.

The computed synthetic spectra can be used to study the detailed behavior of the emission and absorption throughout the solar atmosphere. In particular, in this work we are interested in the amount of local emission at different atmospheric heights for the millimeter–infrared wavelength range. We focus at 17, 212, and 405 GHz, because these are the observing frequencies of the Nobeyama Radio Heliograph (NoRH; Nakajima et al. 1995) and the Solar Submillimeter Telescope (SST; Kaufmann et al. 2008). For this, we use NLTE computations for hydrogen and H^- ion, taking into account three opacity functions (bremsstrahlung, H^- , and inverse bremsstrahlung) for 20 ion species in different ionization stages.

The goal of this work is to compare the common synthetic spectra obtained by using the bremsstrahlung opacity function only with fully ionized atmosphere and a more realistic spectra calculated by using NLTE and three opacity functions, computed with high spatial resolution (of around 1 km).

The three opacity functions, the computation of ionization stages of 20 ion species considering H , H^- , and n_e in NLTE are included in our new model called “Celestun.”

2. OPACITY FUNCTIONS

In order to include the contribution of different ion species, we use the following (complete) opacity function which resumes the slightly different expressions for the bremsstrahlung opacity reported in the literature (Kurucz 1979; Dulk 1985; Rybicki & Lightman 1986; Zheleznyakov 1996):

$$\kappa_{\text{ff}}^n(T, \nu) = \sum_{\xi} \frac{2^{5/2} \sqrt{\pi}}{3\sqrt{3}} \frac{e^6}{c(mk)^{3/2}} \frac{Z_{\xi}^2}{T^{3/2} \nu^2} n_e n_{\xi} \bar{g}_{\text{ff}}(Z_{\xi}, T, \nu), \quad (1)$$

where e is the electron charge, c is the velocity of light, m is the electron mass, k is the Boltzmann constant, Z_{ξ} is the charge of the ion species ξ , T is the electron temperature, ν is the frequency, n_e is the electron density, n_{ξ} is the density of the ion species ξ , and $\bar{g}_{\text{ff}}(Z_{\xi}, T, \nu)$ is the average free–free Gaunt factor which takes into account the initial and final quantum energy states of the total momentum.

The rigorous quantum mechanical expression for the Gaunt factor has been derived by Sommerfeld & Maue (1935) but the solution is difficult to compute and, therefore, many approximations have been developed in order to make the computation easier (see Brussaard & van de Hulst 1962 for a review of average Gaunt factor in the bremsstrahlung opacity function).

Following Rybicki & Lightman (1986), we compute the average free–free Gaunt factor for chromospheric conditions

as

$$\bar{g}_{\text{ff}}(T, Z, \nu) = \begin{cases} \frac{\sqrt{3}}{\pi} \ln \left[\frac{4}{\xi^{5/2} y} x^{1/2} \right] & x < 1, y < g(x) \\ 1, & x \leq 1, y > g(x), y \leq h(x) \\ \left[\frac{12}{xy} \right]^{1/2} & x \leq 1, y > h(x) \\ \frac{\sqrt{3}}{\pi} \ln \left[\frac{4}{y\xi} \right] & x > 1, y < 1 \\ \left[\frac{3}{\pi y} \right]^{1/2} & x > 1, y \geq 1 \end{cases} \quad (2)$$

where

$$x = \frac{kT}{Z^2 \text{Ry}}, \quad (3)$$

$\text{Ry} = 13.6 \text{ eV}$ is the Rydberg constant, and

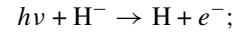
$$y = \frac{h\nu}{kT}, \quad (4)$$

$$g(x) = \frac{9999}{10^4} \left(\frac{99}{10^2} x + \frac{99}{10^3} \right), \quad (5)$$

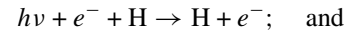
$$h(x) = 1001 - 1000x. \quad (6)$$

Under chromospheric conditions, it is necessary to include the contribution of the H^- ion in the opacity expression. This contribution is effective through three mechanisms (John 1988; Golovinskii & Zon 1980):

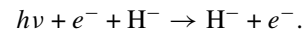
1. The Wildt’s photo-detachment mechanism (Wildt 1939)



2. The neutral interaction (Zheleznyakov 1996)



3. The bremsstrahlung for H^- or inverse bremsstrahlung (Golovinskii & Zon 1980)



In the millimeter–sub-millimeter wavelength range, the photo-detachment mechanism is not relevant (Alexander & Ferguson 1994), whereas the neutral interaction is very important. The corresponding opacity function is

$$\kappa_{\text{ni}}^H = k_{\nu}^{\text{tot}} P_e n_H,$$

where k_{ν}^{tot} is the total absorption coefficient published in John (1988), P_e is the electronic pressure, and n_H is the hydrogen density. Finally, in the wavelength range of interest, the inverse bremsstrahlung opacity is the same as the positive ion case (Golovinskii & Zon 1980; we use bremsstrahlung with $n_i = n_{H^-}$).

Therefore, the total opacity used to compute the synthetic spectrum is

$$\kappa_{\text{ff}} = \kappa_{\text{ff}}^n + \kappa_{\text{ni}}^H + \kappa_{\text{ff}}^{H^-}.$$

3. DENSITY PROFILES

As input parameters, PAKALMPI needs the hydrogen density, the temperature, and the departure coefficients for each layer of the atmospheric model (see Section 3.3). With this profile, PAKALMPI computes the ionic and electronic densities for each layer of the atmospheric model following the derivation of Vernazza et al. (1973), but using more number of energy levels

for each ion, i.e., the Saha equation is solved for the base state and for high energy levels of each ion. For this reason, we define the ionization contribution function (Z function) by

$$Z = \sum_{\xi=\text{He}}^{\Xi} \sum_{N_{\xi}=1}^F N_{\xi} n_{\xi, N_{\xi}}, \quad (7)$$

where

$$\xi = \{\text{H, He, Li, Na, K, } \dots, \Xi\}$$

are the atoms considered in the model, N_{ξ} is the ionization level, $n_{\xi, N_{\xi}}$ is the density of the atom ξ in the ionization level N_{ξ} , and F is the highest energy level for each ion. In order to calculate the Z function, we need an atomic model and the relative density or abundance of each atom. Although the relative density may depend of the atmospheric height, in a first approximation, we assume a constant relative density for all the atmospheric layers.

3.1. Electron Density

In Vernazza et al. (1973), we found the formulas for the electron density which takes into account NLTE computations and uses the fundamental energy state for the ions. However, using our definition of ionization contribution function (Equation (7)), we have

$$n_e = \frac{-(1 - Zd) + \sqrt{(1 - Zd)^2 + 4d(n_H Z)}}{2d}, \quad (8)$$

where n_H is the hydrogen density, Z is the ionization contribution function, T is the temperature, and d is the NLTE contribution function.

3.2. Ion Density

To compute $n_{\xi, N_{\xi}}$, we solve the matrix for the classical Saha equation:

$$\log \frac{n_{\xi, N_{\xi+1}}}{n_{\xi, N_{\xi}}} = -0.1761 - \log(P_e) + \log \frac{u_{N_{\xi+1}}}{u_{N_{\xi}}} + 2.5 \log T - \chi_{\xi, N_{\xi}, k} \frac{5040}{T}, \quad (9)$$

where

$$u_{N_{\xi}} = \sum_n g_{\xi, N_{\xi}} \exp\left(-\frac{\chi_{\xi, N_{\xi}, k}}{kT}\right). \quad (10)$$

PAKALMPI can use a single model of atoms but is able to manage different atomic densities in each layer. Even more, it is possible to change the metallicity in each layer of the atmosphere. In this work, we use the atomic model published by Vernazza et al. (1973).

To calculate the density of H^- we use the following expression (Vernazza et al. 1973):

$$n_{\text{H}^-} = 1.0345 \times 10^{-16} b_{\text{H}^-} n_e n_{\text{H}_1} T^{-3/2} e^{8762/T}.$$

3.3. NLTE Contribution Function

The NLTE contribution function is

$$d = b_1 \psi(T) \left(1 + \sum_{l=2}^N \frac{n_l}{n_1}\right), \quad (11)$$

where the term $\sum_{l=2}^N \frac{n_l}{n_1} \ll 1$ (Vernazza et al. 1973), so that

$$d = b_1 \psi(T), \quad (12)$$

where

$$\psi(T) = \left(\frac{h^2}{2\pi m k T}\right)^{3/2} \exp(\chi_{\text{H}}/kT), \quad (13)$$

and the departure coefficient for hydrogen in the fundamental state (b_1) defined in Menzel (1937) and modified by Vernazza et al. (1973) is

$$b_1 = \frac{n_1/n_1^*}{n_k/n_k^*},$$

where the ratio n_1^*/n_k^* is given by the Saha equation in thermodynamical equilibrium.

As b_1 is difficult to compute for each specific atmospheric layer, and due to the fact that there are only few published atmospheric models reporting this parameter, we have developed an algorithm to obtain an approximation of the departure coefficient based on any published b_1 coefficients.

We found that different theoretical models of the chromosphere are very close to each other when plotted in the dynamic space (density versus temperature, the analysis in the dynamic space is important because, in this space, the problem of the ambiguity between height and temperature is avoided, this is, when the temperature profile has two or more associated heights for a single temperature point). Therefore, it should be easy to get new approximated b_1 parameters from published departure coefficients. If we have two models: a published model (model A) of the atmosphere with temperature $T_A(h)$, density $H_A(h)$, and departure coefficient parameter $b_1(h)$, where h is the height over the photosphere, and a new model (model B) with temperature $T_B(h)$ and density $H_B(h)$, we can approximate b_1 from model A as follows.

1. At a given height over the photosphere (h_B), we take the temperature and density from model B:

$$\vec{p}_B = (T_B(h_B), H_B(h_B)).$$

2. With \vec{p}_B we found the closer point $\vec{p}_A = (T_A(h_A), H_A(h_A))$ to model A (in the dynamic space). This point has an associated height (h_A) over the photosphere in model A.
3. We take the points that enclose h_A

$$[h_0, h_A, h_1]$$

in the same model A.

4. With h_0 and h_1 we can evaluate b_1 in model A in order to interpolate h_A :

$$b_1(h_B) \approx b_1(h_A) = \frac{b_1(h_1) - b_1(h_0)}{h_1 - h_0} (h_A - h_0) + b_1(h_0). \quad (14)$$

By construction, \vec{p}_A and \vec{p}_B have similar physical conditions. Therefore, the computed departure parameter $b_1(h_B)$ can be used in model B with a high degree of confidence. This process is applied to all points in model B to obtain the required approximation for the departure parameters.

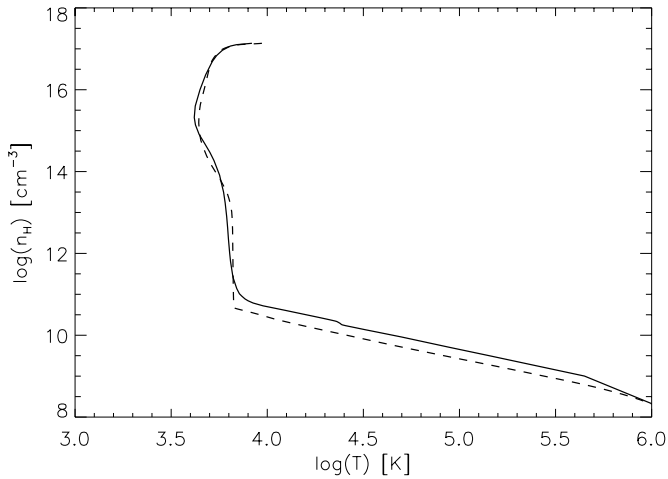


Figure 1. Temperature vs. hydrogen density for VALC model (solid line) and C07 model (dashed line) in the dynamic space.

4. RADIATIVE TRANSFER EQUATION

The local emission, or the emission in a given atmospheric layer, can be represented in the following way:

$$I_{\text{local}} = \epsilon_{\text{abs}} + \epsilon_{\text{emi}} \quad (15)$$

where

$$\epsilon_{\text{abs}} = I_0 \exp(-\tau_{\text{local}}) \quad (16)$$

is the local absorption and

$$\epsilon_{\text{emi}} = S_{\text{local}}(1 - \exp(-\tau_{\text{local}})) \quad (17)$$

is the local emissivity.

In this case, I_0 is the incoming emission from the background (lower adjacent atmospheric layer), τ_{local} is the local optical depth, and S_{local} is the local source function.

We use an updated version of the PAKAL code to solve the radiative transfer equation (De la Luz et al. 2010) along a ray path using an iterative method to compute I_0 and I_{local} .

ϵ_{abs} and ϵ_{emi} are useful to analyze the behavior of the local emissivity of the atmospheric layers. While ϵ_{abs} is related to the level of opacity of a given layer, ϵ_{emi} indicates the capacity of this layer to produce radiation.

With this definition of the radiative transfer equation, we can study in detail the local emission and absorption processes.

5. ALGORITHM

The code PAKALMPI performs the following steps to compute the emission I_ν .

1. Reads the temperature, hydrogen density, and the atomic models for a given layer from the atmospheric pre-calculated model (VALC, C07, etc.),
2. Solves the matrix of the Saha equation (Equation (9)). The solution of the matrix is a set of density of ions for each atomic species considered in this layer.
3. Finds the “Z” contribution of electrons in LTE (Equation (7)).
4. Computes the approximation to the b_1 parameter using the temperature and density of the specific layer.
5. Using b_1 and Z, computes the initial values of n_e (Equation (8)) and n_i .

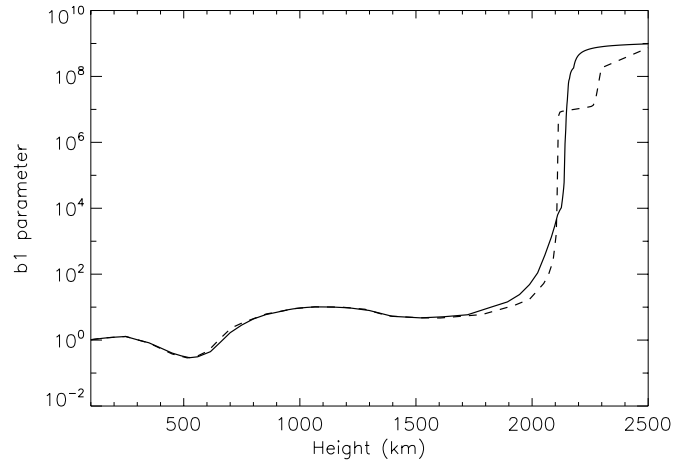


Figure 2. Departure coefficients for VALC (dashed line) and C07 (continue line) approximated model taking into account the b_1 parameter published in the VALC model. We note that for both models b_1 parameter follow the radial temperature. The main differences are seen above 1500 km over the photosphere.

6. Computes n_{H^-} and recalculates n_e and n_{H^1} (this step is necessary since the computation of n_{H^-} needs the electron and neutral hydrogen densities).

These steps are repeated recursively until n_e converges. The iterative process is necessary because we are searching for the equilibrium of the physical system.

Once n_e has converged, the results for all ions are saved and the code gets the temperature, hydrogen density, and abundances for the next layer. In this way, the code produces tables with height profiles of the electron and ion densities.

When all the atmospheric layers have been calculated, PAKALMPI computes the ray trajectory (from the Sun to the observer) and the intersection of this ray path with the radial models (ions, temperature and electronic density) from the computed tables. Finally, PAKALMPI solves the radiative transfer equation using all the considered opacity functions.

The process is repeated (for each ray trajectory) to create two-dimensional images at several frequencies. In this way, PAKALMPI improves the construction of two-dimensional images considering detailed three-dimensional emitting structures.

6. CHROMOSPHERIC SPECTRA

As inputs to our code, we use two complementary atmospheric models: the chromospheric model C07 (Avrett & Loeser 2008) which includes temperature and hydrogen density but does not include the departure coefficients, and the VALC model (Vernazza et al. 1981) in order to get these departure coefficients.

The (atmospheric) plasma behavior can be easily visualized by plotting the plasma density versus the temperature; this is the dynamic space. Therefore, in Figure 1 we have plotted the neutral hydrogen density as a function of temperature for VALC and C07 models. We note that the differences between both models are minimal. This gave us confidence to use both: the C07 atmospheric model in order to get hydrogen density and temperature; and the departure coefficients for the fundamental state of H (b_1) and H^- (b_{H^-}) which are interpolated from the VALC model using our approximation method (Section 3.3). The result is seen in Figure 2, where we have plotted the original departure coefficients (VALC) with a dashed line and our interpolation (for C07) with a continuous line. The main differences correspond to the region of the

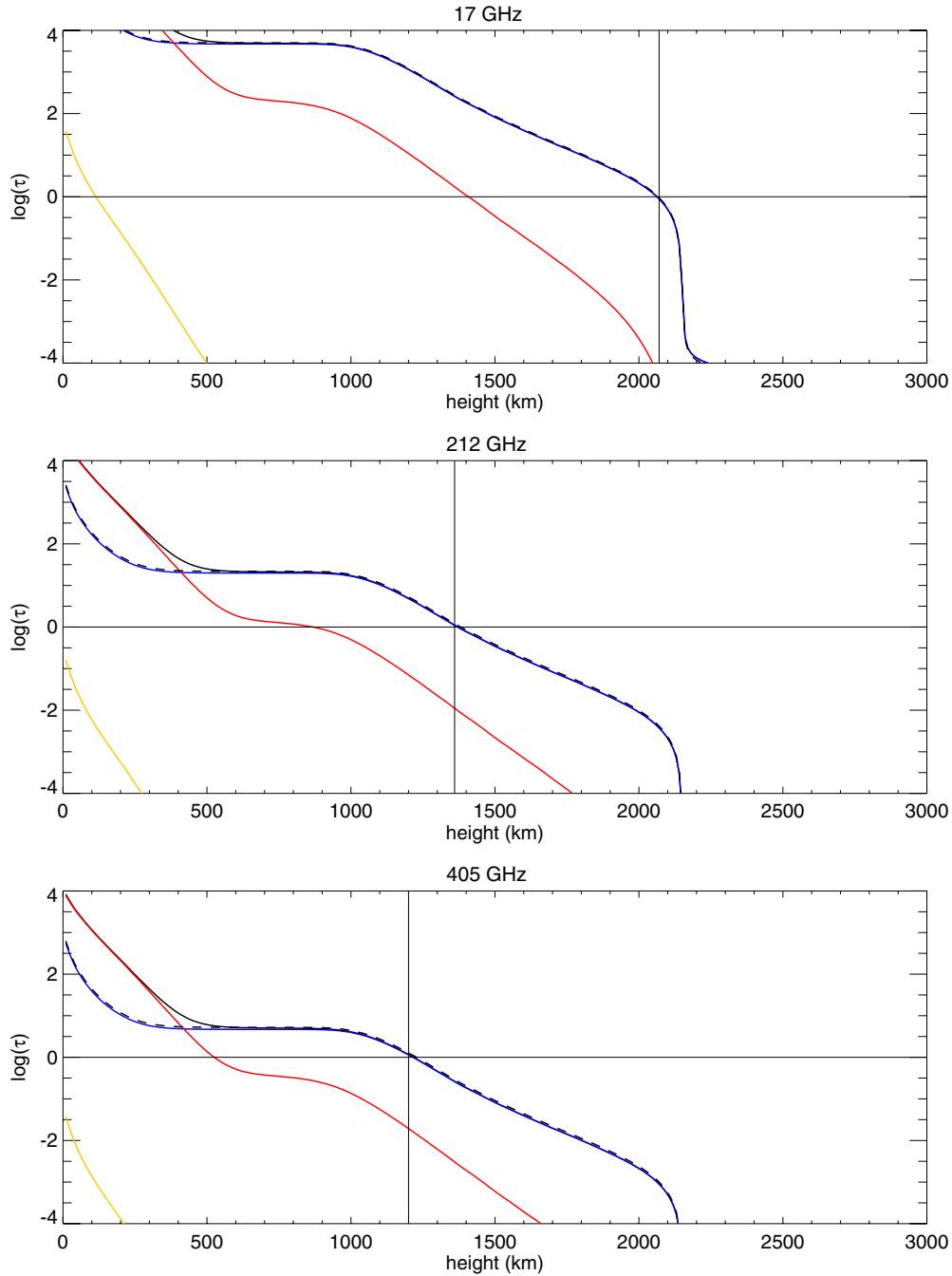


Figure 3. Optical depth at 17, 212, and 405 GHz using the C07 input atmospheric model. In blue we show the contribution of the bremsstrahlung opacity, in red H^- , and in yellow the inverse bremsstrahlung. The continuous line shows the sum of all the contributions, and the dashed line represents only the bremsstrahlung opacity function.

(A color version of this figure is available in the online journal.)

temperature minimum and the transition region, and are caused by temperature differences between both models.

Our code output gives us detailed information of the radiation parameters. For instance, in Figure 3, we show the computed optical depth at 17 GHz (top), 212 GHz (middle), and 405 GHz (bottom) as a function of radial height. We made two simulations: the first one using only bremsstrahlung opacity (dashed black lines); and the second one using our model Celestun; in this case, the yellow lines represent the inverse bremsstrahlung opacity, the H^- opacity is shown by red lines, the blue lines correspond to the classical bremsstrahlung opac-

ity, and the black continuous lines represent the full opacity function from Celestun. The introduction of H^- and inverse bremsstrahlung opacities does not change the height where the atmosphere becomes optically thick ($\tau \sim 1$). However, it is clear that below 500 km, the H^- process is the major source of opacity in the solar atmosphere.

The detailed local behavior of the emission at 17, 212, and 405 GHz is seen in Figure 4, where we have plotted the brightness temperature (black lines) and the input atmospheric radial temperature (yellow lines) as a function of the atmospheric height. The continuous and dashed lines represent,

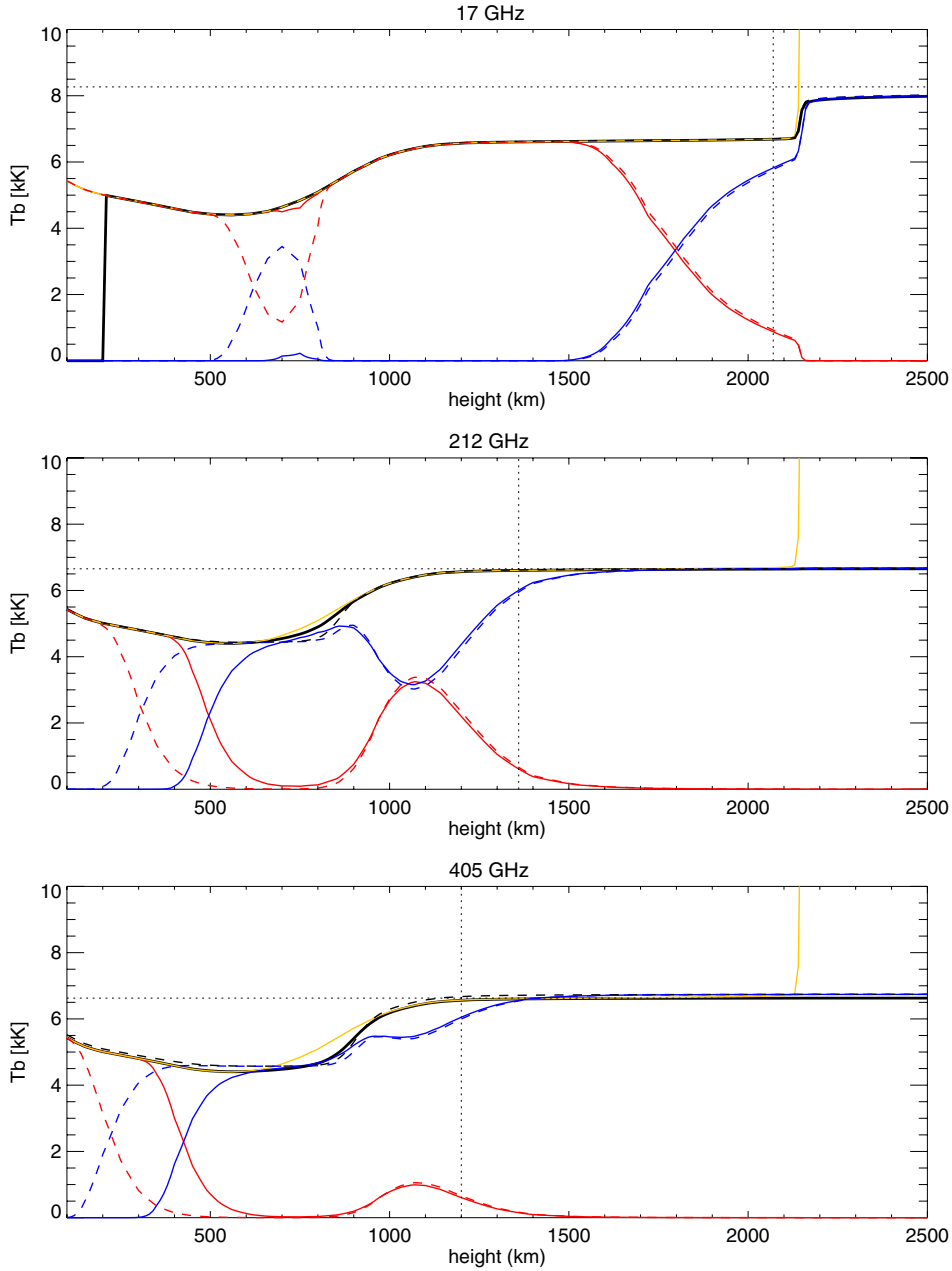


Figure 4. Local absorption (ϵ_{abs} , blue) and local emissivity (ϵ_{emi} , red) for 17, 212, and 405 GHz (top to bottom) using the C07 input atmospheric model. In yellow we show the radial temperature and in black the brightness temperature.

(A color version of this figure is available in the online journal.)

respectively, the cases where all, and only bremsstrahlung opacities were considered. The contribution, to the local brightness, of the absorption ϵ_{abs} (Equation (16)) is plotted in blue, whereas the emission ϵ_{emi} (Equation (17)) is plotted in red.

We note that there are two separate regions where clearly the emission has a significant contribution: the first one is close to the photosphere, and it is interesting to note that the height of this region increases when the H^- opacity function is considered; the importance of the second enhanced emission region decreases with frequency, and the H^- opacity does not produce any differences in this region. The second enhanced region and the H^- opacity do not affect the final brightness temperature, which is why these structures were unnoticed until now. The contribution of the inverse bremsstrahlung is negligible.

7. SYNTHETIC SPECTRA

It is interesting to compare the output of our code using different input atmospheric models. For instance, in Figure 5, we show observations performed at different phases of the solar cycle and collected by Loukitcheva et al. (2004): diamonds correspond to close-to-minimum, the square symbols to intermediate, and triangles to close-to-maximum phases of the solar cycle. In the same figure, we have plotted the synthetic solar spectra computed using all (continuous lines) and only bremsstrahlung (dashed lines) opacities and the following input models: VALC as yellow lines, CAIUS05 (Selhorst et al. 2005) as blue lines, C7 as black lines, and again CAIUS05 but using their electronic density and physical assumptions (bremsstrahlung opacity and fully ionized atmosphere) as red lines.

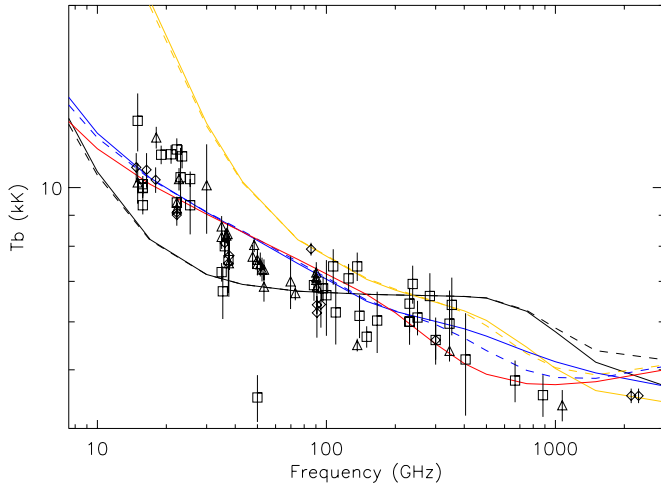


Figure 5. Synthetic solar spectra and observations at different stages of solar activity cycle, collected by Loukitcheva et al. (2004). The square points are intermediate, diamonds close-to-minimum, and triangles close-to-maximum of the solar activity cycle. The solar spectra are shown for bremsstrahlung opacity (dashed line) and Celestun model (continuous line) for four input atmospheric models: C7 (black), SEL05 (blue), VALC (yellow), and SEL05 but using their electronic density (red).

(A color version of this figure is available in the online journal.)

There are interesting differences in the input atmospheric models, e.g., the altitude and the length of the chromospheric temperature minimum, as well as the altitude and the morphology of the chromospheric upper limit (i.e., the beginning of the transition zone and corona). The VALC model has the temperature minimum closer to the photosphere and is the warmest. This model has a thin chromosphere and defines a “plateau zone,” where the chromosphere temperature reaches 20,000 K. This plateau is responsible of the high brightness temperature at low frequencies (see Figure 5 and de La Luz et al. 2008). The CAIUS05 model has a similar altitude for the temperature minimum but is hotter and shorter compared to the VALC model. The chromospheric temperature grows exponentially up to coronal values. The CAIUS05 model has the largest chromosphere. The C7 model has the lowest temperature minimum, and then a constant temperature until the rise due to the transition region and the corona. This model eliminates the plateau zone using ambipolar diffusion.

In order to facilitate the analysis, we separately consider three regions of the spectrum: from 2 to 60 GHz (low frequency), from 60 to 400 GHz (intermediate frequency), and from 400 GHz to 3 THz (high frequency).

At low frequency range, the temperature differences of the atmospheric models produce significant differences in the spectra (regardless of the opacity function), this emitting region is located at the upper chromosphere ~ 1500 km over the photosphere. For intermediate frequencies, the simulations agree rather well with the observations, however, the observations have large dispersion. Finally, at high frequency range, we note that there is an apparent discontinuity at 400 GHz. In this region, the model that fits the observations better is CAIUS05. On the other hand, both C07 and VALC models predict higher brightness temperatures than the observed.

These apparent minimal differences between input atmospheric models produce significant differences in the resultant synthetic spectra computed from our radiative model.

8. DISCUSSION AND CONCLUSIONS

Using different atmospheric models and opacity functions, we have computed the optical depth, τ , at low atmospheric altitudes. Our results show that if we use either, only bremsstrahlung or Celestun (i.e., H, H^- , and inverse bremsstrahlung) opacities, the height over the photosphere where the overlying atmosphere becomes optically thick ($\tau \approx 1$) remains unalterable. However, if we take into account the local emissivity (Equation (17)) we show that the height, where the main emission is generated, changes meaningfully.

For example, at 17 GHz the height over the photosphere where the atmosphere starts to become optically thin is around 1500 km, but the height where $\tau = 1$ is around 2050 km. There are local emissivity structures below 1500 km, although they remain invisible to the observer because the atmosphere is optically thick at these heights. When we considered bremsstrahlung opacity only, the local emissivity at 17 GHz changes in a region between 500 and 850 km over the photosphere (the atmosphere becomes optically thin). This structure is not present when the Celestun model is considered.

At 212 and 405 GHz the behavior of the local emissivity changes noticeably, since at these frequencies two regions of emissivity are present: a lower one, closer to the photosphere shows deep differences when comparing between both models. The height of the region where the emission is generated is higher by 200 km when the Celestun model is used. The uppermost region is located between 800 and 1500 km above the photosphere. In this region, there is no difference between the two models. As seen in Figure 4, the second layer of emission is below $\tau = 1$ height and is similar for both models. Even more, after 1000 km, the brightness temperature remains unalterable. This is due to the fact that the temperature of the atmospheric model is the upper limit for the brightness temperature and remains constant between 1000 and 2000 km above the photosphere. The brightness temperature remains unalterable. These facts mask the local emission processes which are unnoticed by the observer.

We found that the dominant emission mechanism changes with altitude: H^- is dominant below 500 km whereas bremsstrahlung dominates at upper heights, although the final brightness temperature remains unchanged.

Our results show that the inclusion of the H^- and inverse bremsstrahlung mechanisms does not modify the final brightness temperature. But the H^- opacity function has a significant impact on the local emissivity and absorbcency, and it must be considered when studying micro-structures in the low chromosphere. Therefore, the Celestun code is a valuable tool for performing this kind of studies. The inverse bremsstrahlung has no impact on the brightness temperature, neither on the local emissivity nor on the absorbcency processes.

We note that there are more emission mechanisms acting at the low solar atmosphere, for instance, molecular emission has been reported for CO (Solanki et al. 1994) and also in the 515.60–516.20 nm spectral range (C_2 and MgH; Faurobert & Arnaud 2002). The emitting layer is situated below the 1100 km, making it evident that these molecules are present in a thin layer inside the temperature minimum region between the photosphere and the low chromosphere. However, observations in visible wavelengths have shown that the molecular emission at the limb-brightening region is negligible, corresponding to 0.2% of the continuum intensity at the center of the solar disk. Nevertheless, a detailed study of the contribution of the molecular rotational spectrum at these wavelengths is necessary.

Although our simulations are related to quiescent solar situations, the next natural steps will be to investigate and compare with flaring cases. Therefore, such research could in principle be used to better understand the thermal structure of the flaring solar atmosphere, that is the response of the atmosphere to flare energy release. From the few existing semi-empirical flare models like Machado et al. (1980) and Mauas et al. (1990), we should grossly expect decreasing radio fluxes as a function of increasing wavelengths in the range from centimeter to far-infrared wavelengths.

We will pay special attention to the density structure of the flaring loops (due to its importance in the computed opacity functions). It is clear that new simulations, observations, and their comparison are needed to better investigate the structure and dynamics of the low layers of the solar atmosphere during flares.

Part of this work was supported by UNAM-PAPPIT IN117309-3 and CONACyT 24879 grants. Thanks to the National Center of Supercomputing in Mexico for allowing us to use their computer facilities and Dr. Emanuele Bertone for comments. J.P.R. thanks CNPq agency (Proc. 305655/2010-8). Thanks to Professor Pierre Kaufmann, director of CRAAM-Centro de Rádio Astronomia e Astrofísica Mackenzie, where part of this research was performed.

REFERENCES

- Ahmad, I. A., & Kundu, M. R. 1981, *Sol. Phys.*, **69**, 273
 Alexander, D. R., & Ferguson, J. W. 1994, *ApJ*, **437**, 879
 Athay, R. G., & Thomas, R. N. 1961, *Physics of the Solar Chromosphere* (New York: Interscience)
- Avrett, E. H., & Loeser, R. 2008, *ApJS*, **175**, 229
 Ayres, T. R. 1989, *Sol. Phys.*, **124**, 15
 Brussaard, P. J., & van de Hulst, H. C. 1962, *Rev. Mod. Phys.*, **34**, 507
 Chiuderi, C., & Chiuderi Drago, F. 2004, *A&A*, **422**, 331
 Chiuderi Drago, F., Kundu, M. R., & Schmahl, E. J. 1983, *Sol. Phys.*, **85**, 237
 Cillié, G. G., & Menzel, D. H. 1935, *Harvard College Obs. Circ.*, **410**, 1
 de La Luz, V., Lara, A., Mendoza, E., & Shimojo, M. 2008, *Geofis. Int.*, **47**, 197
 De la Luz, V., Lara, A., Mendoza-Torres, J. E., & Selhorst, C. L. 2010, *ApJS*, **188**, 437
 Dulk, G. A. 1985, *ARA&A*, **23**, 169
 Faurobert, M., & Arnaud, J. 2002, *A&A*, **382**, L17
 Giovanelli, R. G. 1949, *MNRAS*, **109**, 298
 Golovinskii, P. A., & Zon, B. A. 1980, *Zh. Tekh. Fiz.*, **50**, 1847
 John, T. L. 1988, *A&A*, **193**, 189
 Kaufmann, P., et al. 2008, *Proc. SPIE*, **7012**, 70120L
 Kundu, M. R. 1970, *Sol. Phys.*, **13**, 348
 Kurucz, R. L. 1979, *ApJS*, **40**, 1
 Kuznetsova, N. A. 1978, *SvA*, **22**, 345
 Landi, E., & Chiuderi Drago, F. 2003, *ApJ*, **589**, 1054
 Loukitcheva, M., Solanki, S. K., Carlsson, M., & Stein, R. F. 2004, *A&A*, **419**, 747
 Machado, M. E., Avrett, E. H., Vernazza, J. E., & Noyes, R. W. 1980, *ApJ*, **242**, 336
 Mauas, P. J. D., Machado, M. E., & Avrett, E. H. 1990, *ApJ*, **360**, 715
 Menzel, D. H. 1937, *ApJ*, **85**, 330
 Nakajima, H., et al. 1995, *J. Astrophys. Astron. Suppl.*, **16**, 437
 Raulin, J.-P., & Pacini, A. A. 2005, *Adv. Space Res.*, **35**, 739
 Rybicki, G. B., & Lightman, A. P. (ed.) 1986, *Radiative Processes in Astrophysics* (New York: Wiley), 400
 Selhorst, C. L., Silva, A. V. R., & Costa, J. E. R. 2005, *A&A*, **433**, 365
 Solanki, S. K., Livingston, W., & Ayres, T. 1994, *Science*, **263**, 64
 Sommerfeld, A., & Maue, A. W. 1935, *Ann. Phys., Lpz.*, **415**, 589
 Vernazza, J. E., Avrett, E. H., & Loeser, R. 1973, *ApJ*, **184**, 605
 Vernazza, J. E., Avrett, E. H., & Loeser, R. 1976, *ApJS*, **30**, 1
 Vernazza, J. E., Avrett, E. H., & Loeser, R. 1981, *ApJS*, **45**, 635
 Wildt, R. 1939, *ApJ*, **90**, 611
 Zheleznyakov, V. V. (ed.) 1996, *Radiation in Astrophysical Plasmas* (Astrophysics and Space Science Library, Vol. 204; Dordrecht: Kluwer)

ERRATUM: “SYNTHETIC SPECTRA OF RADIO, MILLIMETER, SUB-MILLIMETER, AND INFRARED REGIMES WITH NON-LOCAL THERMODYNAMIC EQUILIBRIUM APPROXIMATION” (2011, APJ, 737, 1)

VICTOR DE LA LUZ¹, ALEJANDRO LARA², AND JEAN-PIERRE RAULIN³

¹ SCiESMEX, Instituto de Geofísica, Unidad Michoacan, Universidad Nacional Autónoma de México, Morelia, Michoacan, México. CP 58190; vdelaluz@geofisica.unam.mx

² Instituto de Geofísica, Universidad Nacional Autónoma de México 04510, México

³ CRAAM, Universidade Presbiteriana Mackenzie, Sao Paulo, SP, 01302-907, Brazil
Received 2015 January 17; accepted 2015 January 20; published 2015 April 2

In Figure 3, we found an incorrect scale for the optical depth (τ), which shows lower values than computed with our algorithm. We provide a replacement figure with the corrected scale.

It does not affect the results and discussion in the published version of this paper.

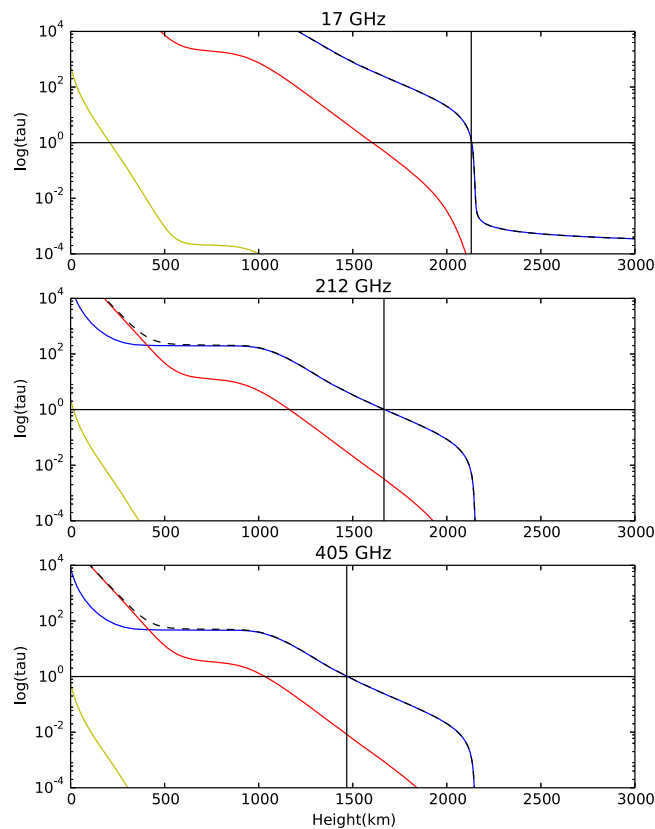


Figure 3. Optical depth at 17, 212, and 405 GHz using the C07 input atmospheric model. In blue we show the contribution of the bremsstrahlung opacity, in red H, and in yellow the inverse bremsstrahlung. The continuous line shows the sum of all the contributions, and the dashed line represents only the bremsstrahlung opacity function.